



FAST Observations of an Extremely Active Episode of FRB 20201124A. II. Energy Distribution

Yong-Kun Zhang^{1,2,3} , Pei Wang¹, Yi Feng³, Bing Zhang^{4,5}, Di Li^{1,2,3,6}, Chao-Wei Tsai¹, Chen-Hui Niu¹, Rui Luo⁷ ,
Ju-Mei Yao⁸, Wei-Wei Zhu¹, Jin-Lin Han^{1,2}, Ke-Jia Lee⁹, De-Jiang Zhou^{1,2} , Jia-Rui Niu^{1,2} , Jin-Chen Jiang⁹ ,
Wei-Yang Wang^{9,10}, Chun-Feng Zhang⁹, Heng Xu⁹, Bo-Jun Wang⁹, and Jiang-Wei Xu⁹

¹ National Astronomical Observatories, Chinese Academy of Sciences, Beijing 100101, China; dili@nao.cas.cn

² University of Chinese Academy of Sciences, Beijing 100049, China

³ Research Center for Intelligent Computing Platforms, Zhejiang Laboratory, Hangzhou 311100, China

⁴ Department of Physics and Astronomy, University of Nevada, Las Vegas, NV 89154, USA; bing.zhang@unlv.edu

⁵ Nevada Center for Astrophysics, University of Nevada, Las Vegas, NV 89154, USA

⁶ NAOC-UKZN Computational Astrophysics Centre, University of KwaZulu-Natal, Durban 4000, South Africa

⁷ CSIRO Space and Astronomy, PO Box 76, Epping, NSW 1710, Australia

⁸ Xinjiang Astronomical Observatory, Chinese Academy of Sciences, Urumqi 830011, China

⁹ Kavli Institute for Astronomy and Astrophysics, Peking University, Beijing 100871, China

¹⁰ Department of Astronomy, Peking University, Beijing 100871, China

Received 2022 June 30; revised 2022 September 17; accepted 2022 September 20; published 2022 November 30

Abstract

We report the properties of more than 800 bursts detected from the repeating fast radio burst (FRB) source FRB 20201124A with the Five-hundred-meter Aperture Spherical radio Telescope (FAST) during an extremely active episode on UTC 2021 September 25–28 in a series of four papers. In this second paper of the series, we study the energy distribution of 881 bursts (defined as significant signals separated by dips down to the noise level) detected in the first four days of our 19 hr observational campaign spanning 17 days. The event rate initially increased exponentially but the source activity stopped within 24 hr after the 4th day. The detection of 542 bursts in one hour during the fourth day marked the highest event rate detected from one single FRB source so far. The bursts have complex structures in the time-frequency space. We find a double-peak distribution of the waiting time, which can be modeled with two log-normal functions peaking at 51.22 ms and 10.05 s, respectively. Compared with the emission from a previous active episode of the source detected with FAST, the second distribution peak time is smaller, suggesting that this peak is defined by the activity level of the source. We calculate the isotropic energy of the bursts using both a partial bandwidth and a full bandwidth and find that the energy distribution is not significantly changed. We find that an exponentially connected broken-power law function can fit the cumulative burst energy distribution well, with the lower and higher-energy indices being -1.22 ± 0.01 and -4.27 ± 0.23 , respectively. Assuming a radio radiative efficiency of $\eta_r = 10^{-4}$, the total isotropic energy of the bursts released during the four days when the source was active is already 3.9×10^{46} erg, exceeding $\sim 23\%$ of the available magnetar dipolar magnetic energy. This challenges the magnetar models which invoke an inefficient radio emission (e.g., synchrotron maser models).

Key words: (stars:) pulsars: general – stars: individual (FRB 20201124A) – methods: data analysis

Supplementary material for this article is available online

1. Introduction

Fast Radio Bursts (FRBs) are short-duration bright transients in radio band. Since the first discovery (Lorimer et al. 2007), more than 600 FRB sources have been detected (Petroff et al. 2016; CHIME/FRB Collaboration et al. 2021). While most of the FRBs were detected once, more than 20 sources have been observed to emit repeated bursts.¹¹ Whether FRBs can be divided into repeaters and non-repeaters is still an open

question. The engine to power FRB sources and the physical mechanism to generate coherent radio emission are subject to intense study (Zhang 2020).

Emitted energy is a fundamental property of FRBs. For the FRB population, the luminosity function is usually assumed to be a power law function with an exponential high-energy cutoff (also called Schechter function, Schechter 1976). In the literature, the power law index α of the Schechter luminosity function (dN/dL) has been constrained by different groups using different FRB samples (Lu & Kumar 2016, 2019; Bhandari et al. 2018; Luo et al. 2018, 2020; Macquart & Ekers

¹¹ <https://www.wis-tns.org/>

2018; Golpayegani et al. 2019; Zhang et al. 2021; Hashimoto et al. 2022), with α constrained to the range from -1.5 to -2.2 . Lu et al. (2020) showed that an index ~ -1.8 can account for FRBs down to the low-luminosity Galactic FRB 200418. The observed FRB population is a convolution of the luminosity function and redshift distribution. For sources in Euclidean geometry with constant space density, the observed fluence distribution should follow a power law distribution with an index -1.5 (Vedantham et al. 2016). As cosmological sources, FRBs' spatial distribution deviates from this simple law and the unknown redshift distribution may play a role in shaping the observed population. If the progenitors of FRBs are young, the number density of FRBs should track the cosmic star formation history (Madau & Dickinson 2014; Nicholl et al. 2017) toward redshift about $z \sim 2$. Some studies have demonstrated that the FRB samples show the trend of deviating from the star formation history (Hashimoto et al. 2020b; Arcus et al. 2021; Zhang et al. 2021; James et al. 2022). In particular, the Canadian Hydrogen Intensity Mapping Experiment (CHIME) first catalog sample seems to suggest a redshift distribution that is delayed from the star formation history (Hashimoto et al. 2022; Zhang & Zhang 2022), hinting that a good fraction of FRB progenitors are likely old, with the number density decreasing toward high redshift. In any case, various studies confirmed that the derived luminosity/energy functions are consistent with each other regardless of the assumption of redshift distribution (Lu & Kumar 2016, 2019; Bhandari et al. 2018; Luo et al. 2018; Macquart & Ekers 2018; Golpayegani et al. 2019; Luo et al. 2020; Zhang et al. 2021; Hashimoto et al. 2022; Zhang & Zhang 2022).

For repeating FRBs, the energy/luminosity functions of individual sources with hundreds of bursts can be studied in great detail. Detailed studies on the two well-known sources FRB 20121102A and FRB 20180916B suggested that they can be modeled by a power law function with the power law indices ranging from -2.8 to -1.7 for bright bursts (Law et al. 2017; Gourdjji et al. 2019; Wang & Zhang 2019; CHIME/FRB Collaboration et al. 2020; Aggarwal et al. 2021; Cruces et al. 2021). These results can imply some differences for the two kinds of FRBs with respect to luminosity/energy functions (Hashimoto et al. 2020a). Owing to the high sensitivity of the Five-hundred-meter Aperture Spherical radio Telescope (FAST, Nan et al. 2011), Li et al. (2021) revealed a detailed energy function using more than 1600 bursts for the repeater FRB 20121102A. They found that the energy function cannot be fitted with one single power law, but requires a two-component model to fit the data. Besides the rough power law component in the high-energy end, there exists a log-normal low-energy component with characteristic values at $\sim 4.8 \times 10^{37}$ erg. It is unclear whether such a feature is universal among repeaters.

FRB 20201124A was first discovered by the CHIME/FRB Project on 2020 November 24 and entered a high-active period in 2021 March (CHIME/FRB Collaboration et al. 2021). Hundreds

of bursts were reported during this period with a variety of radio telescopes (Hilmarsson et al. 2021; Law et al. 2021; Marthi et al. 2021; Xu et al. 2021; Kumar et al. 2022; Lanman et al. 2022). In particular, our previous FAST observations (Xu et al. 2021) detected 1863 bursts that revealed significant short-term evolution of the rotation measure (RM). Multiple independent follow-up observations with radio interferometers localized this source to a host galaxy, which has a spectroscopic redshift of $z = 0.0979$, corresponding to a luminosity distance of 451 Mpc with $h = 0.7$, $\Omega_\Lambda = 0.7$ and $\Omega_m = 0.3$ (Fong et al. 2021; Piro et al. 2021; Nimmo et al. 2022; Ravi et al. 2022). Follow-up observations using the Keck optical telescope revealed that the host galaxy is a Milky Way-like, metal-rich, barred spiral galaxy with the FRB source residing in a low stellar density, interarm region at an intermediate galactocentric distance (Xu et al. 2021). This source also shows its diversity in the burst properties, such as extremely high brightness and complex structure (Marthi et al. 2021; Kumar et al. 2022), high degree of circular polarization, variation in the polarization position angle (Hilmarsson et al. 2021; Xu et al. 2021; Kumar et al. 2022) and obvious scintillation (Main et al. 2021). This previous active phase lasted until the end of May 2021.

CHIME/FRB reported a new burst from FRB 20201124A on 2021 September 21.¹² Triggered by this event, we started to use FAST to monitor this source since 2021 September 25. The observations lasted until October 17 for a total of 17 days, leading to the detection of more than 700 bursts during the first four days. In this paper, we mainly focus on the energy distribution of FRB 20201124A. The morphology, polarization and periodicity search using the same set of data are discussed in Paper I (Zhou et al. 2022), III (Jiang et al. 2022) and IV (Niu et al. 2022a), respectively. Section 2 describes our observations, burst detection and data reduction procedures. Section 3 elucidates the results of our analysis on the burst energies and the energetics of this source. Section 4 discusses the comparison of the luminosity/energy function between this source and other sources. In Section 5, we present our conclusions.

2. Observations and Data Processing

The observations of FRB 20201124A were carried out from 2021 September 25 to October 17 with a total of 19 hr of observing time, using FAST 19-beam receiver (Li et al. 2018; Jiang et al. 2020), which covers a frequency bandwidth of 1–1.5 GHz.

2.1. Burst Detection

The data recorded by FAST are in FITS format with 4096 frequency channels and a time resolution of $49.152 \mu\text{s}$. We first perform de-dispersion processing on the time-frequency data according to different DM values to construct new time-DM data. We then use the trained object detection model to identify

¹² <https://www.chime-frb.ca/repeaters>

the arrival time and DM of the bursts in the data. According to the DM value and burst arrival time, the data on pulse candidates are cut from the original data, and a binary classification neural network is utilized to determine whether they are true bursts or false signals. We also searched for bursts in dedispersed time series using a matched filtering algorithm as implemented by the PRESTO program (Ransom 2001). We combined the bursts detected by the two search methods as the final sample.

2.2. DM Optimization

Since DM is the integral of electron density along the path, we assume that the DM does not change significantly within an hour. We first use a uniform DM value of 413 pc cm^{-3} to select the pulses detected in one day from the data. Under 8 times down-sampling of time, bursts with a signal-to-noise ratio (S/N) greater than 10 are selected. We then change the DM trials ranging from -5 to 5 pc cm^{-3} from the central value for de-dispersion to maximize the structure of all the burst profiles, and reapply this DM value to all bursts on this day.

2.3. Flux Calibration

For each burst, we estimate the peak flux density with the radiometer equation

$$S_\nu = \frac{\text{SNR} \times T_{\text{sys}}}{G \sqrt{n_p \times \text{BW} \times t_{\text{samp}}}}, \quad (1)$$

where T_{sys} is the system temperature and G is the gain of the telescope, which is modeled as a function of the zenith angle and observation frequency in Jiang et al. (2020), $n_p = 2$ is the number of polarizations summed, t_{samp} is the sampling time and BW is the bandwidth used for calibration.

Repeating FRBs tend to have a narrow emission bandwidth compared with apparent non-repeating events (Pleunis et al. 2021). The bandwidth may be related to the telescope sensitivity. For these narrow band bursts, usually the energy is calculated using the flux density defined by the full bandwidth to be multiplied by the full bandwidth. Alternatively, the energy can be calculated using the flux defined with the narrow band in which the burst is detected and multiplied by this narrow band. We roughly estimate the emission bandwidth of each burst by dividing the whole bandpass into multiple 50 MHz sub-bands and identifying the sub-bands containing burst emission. If the calculations are performed correctly, the two methods should result in the same results. In order to check this, we calculate S_ν using two ways. The first is to assume that the burst energy is spread in the full bandwidth of the telescope $\text{BW} = 500 \text{ MHz}$ for all the bursts. The second is to use the true BW for each individual burst. When different bandwidths are adopted, the noise level and the S/N of a pulse change. Therefore, when utilizing the observed pulse

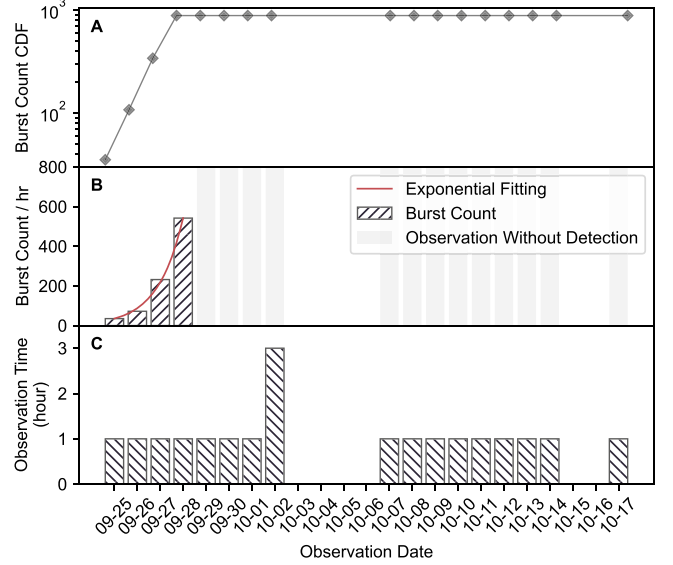


Figure 1. Observation and Detection of FRB 20201124A. A: the cumulative distribution of burst detection. B: the burst count in each observation day. Gray bars are the observation sessions without burst detection, and the red line traces the exponential fitting of the burst detection. C: the length of each observation session.

bandwidth for flux calibration, we recalculated the S/N and the T_{sys} and G of the corresponding frequency bandwidth.

3. Results

3.1. Rate and Waiting Time

During the 17 day observing campaign, we detected 35, 72, 232 and 542 bursts from FRB 20201124A in the first four days respectively (i.e., from September 25 to 28), for a total of 881 bursts. The bursts are defined as significant signals separated by dips down to the noise level in this paper.¹³ Properties of these bursts are listed in the Appendix Table A1. The observation and detection are depicted in Figure 1. The cumulative distribution is plotted in the linear-logarithmic scale. The linear line in the figure suggests that the accumulated number increases exponentially with time. Interestingly, the bursts suddenly disappeared the next day, which was unexpected. The peak burst rate on the third and fourth day reached 232 hr^{-1} and 542 hr^{-1} , respectively, which exceeded all previously reported burst rates from this and other repeating FRBs, including 122 hr^{-1} (Li et al. 2021) and 218 hr^{-1} (Jahns et al. 2022) for FRB 20121102A, 4.5 hr^{-1} for FRB 20190520B (Niu et al. 2022b) and 45.8 hr^{-1} for FRB 20201124A itself during the previous active session (Xu et al. 2021).

Waiting time is defined as the difference between the arrival time of two adjacent bursts. All the waiting times were

¹³ We note that the definitions of a burst are different among the four papers in this series, because different groups adopted different criteria for the different scientific purposes in the respective papers.

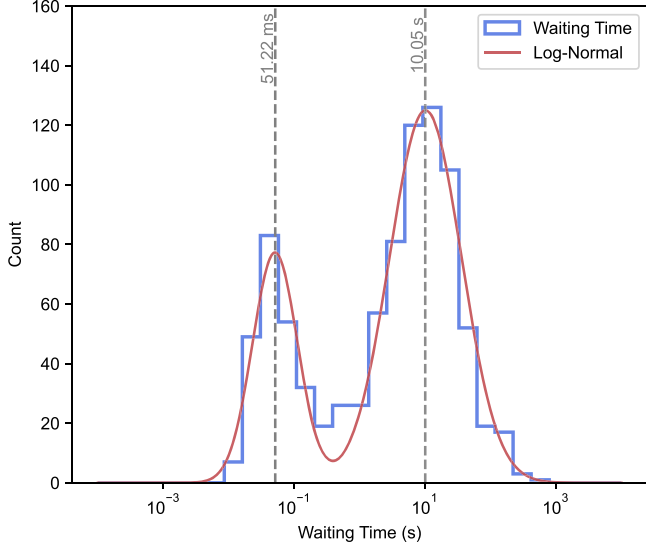


Figure 2. Waiting time distribution of FRB 20201124A. The blue steps and red line represent the distribution of waiting times and two log-normal fittings respectively.

calculated in the same observation session to avoid the observation gap of about 23 hr. The waiting time distribution of FRB 20201124A is plotted in Figure 2, which can be well-fitted by two log-normal functions peaking at 10.05 s and 51.22 ms, respectively. Note that the waiting time distribution of FRB 20201124A in the previous active period was also a bimodal distribution, but the characteristic timescale of the second (long-duration) peak was 135 s (Xu et al. 2021). Our observation suggests that this characteristic waiting time is not universal within one source, but rather depends on the activity level of the source. The bimodal form of waiting time has also been found in FRB 20121102A (Aggarwal et al. 2021; Li et al. 2021; Hewitt et al. 2022). The timescale of the second peak varies also significantly for telescopes with different sensitivities, with shorter waiting times for more sensitive telescopes (which detect more bursts).

3.2. Energy Calculation

We calculate the isotropic equivalent burst energy following the equation

$$E = 10^{39} \text{erg} \frac{4\pi}{1+z} \left(\frac{D_L}{10^{28} \text{cm}} \right)^2 \left(\frac{F_\nu}{\text{Jy} \cdot \text{ms}} \right) \left(\frac{\Delta\nu}{\text{GHz}} \right), \quad (2)$$

where $D_L = 453.3$ Mpc is the luminosity distance of FRB 20201124A corresponding to the redshift $z = 0.09795$ acquired in Xu et al. (2021), $F_\nu = S_\nu \times W_{\text{eq}}$ is the specific fluence, S_ν is the peak specific flux and $\Delta\nu$ is the bandwidth of each pulse. The adoption of $\Delta\nu$ is more relevant for narrow band FRBs, which are typically the case for the bursts in repeaters. As

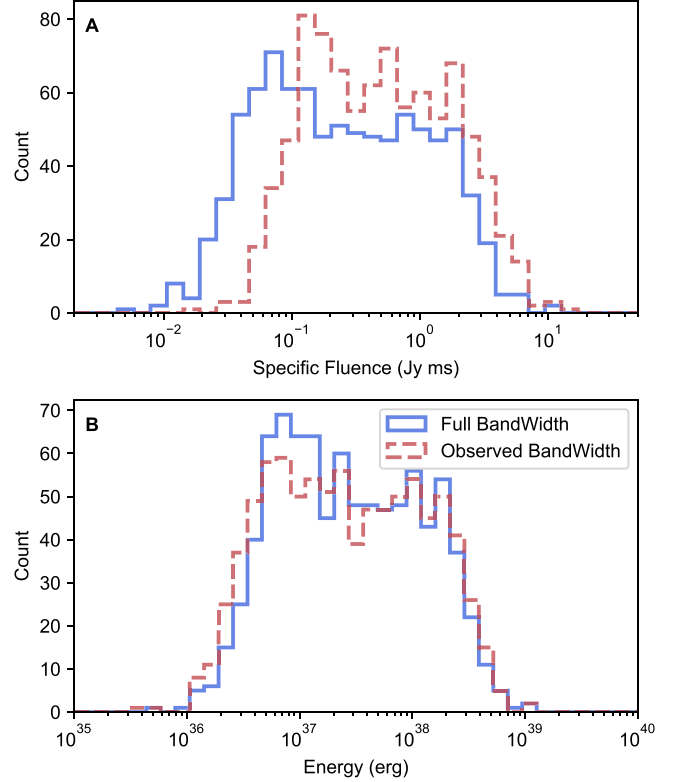


Figure 3. Specific fluence and energy distribution. Energy is calculated by Equation (2). Solid blue lines are distribution for full bandwidth, i.e., $\Delta\nu = 500$ MHz, and red dashed lines are for observed burst bandwidth.

discussed in Section 2.3, we adopt two choices of BW to calculate S_ν and compare the derived E values.

Figure 3(A) features the specific fluence (F_ν) and the energy distribution of bursts calculated with $\Delta\nu = 500$ MHz and the observed bandwidth for individual bursts. The specific fluence derived using the observed narrow bandwidth is greater than that derived assuming the full bandwidth. This is natural because the definition of F_ν is the average over frequency channels. Since the energy contained in the observed bandwidth is similar to that in the full bandwidth but the observed bandwidth is narrower than the full bandwidth, the average value for the full bandwidth is smaller. Figure 3(B) presents the energy distribution of the two methods after multiplying by the respective bandwidth. It can be seen that the derived energy distributions between the two methods appear to be similar to each other, as is expected. The p -value from the Kolmogorov-Smirnov (K-S) test of the energy distribution calculated with two types of bandwidth is 0.35, which cannot reject the hypothesis that the two energy distributions are consistent with each other. Therefore, we conclude that the energy calculation is not significantly affected by the adoption of the bandwidth, and the normal method using the full bandwidth to calculate the energy is reliable.

Table 1
Energy Budget of Three Repeating FRBs

Name	Ob Days (day)	Ob Times T_{obs} (hr)	Total Observed Energy ^a E_{radio} (erg)	Averaged Energy ^b \bar{L}_{radio} (erg s ⁻¹)	Total Energy ^c E_{bursts} (erg)
FRB 20201124A	4	4	1.60×10^{41}	1.11×10^{37}	3.85×10^{46}
FRB 20201124A-0928	1	1	1.02×10^{41}	2.84×10^{37}	2.46×10^{46}
FRB 20121102A	47	59.5	3.41×10^{41}	1.59×10^{36}	6.47×10^{46}
FRB 20190520B	11	18.5	1.10×10^{40}	1.65×10^{35}	1.56×10^{45}

Notes.

^a Sum of the observed isotropic radio energies of all bursts.

^b Defined as $E_{\text{radio}}/T_{\text{obs}}$.

^c $E_{\text{bursts}} = E_{\text{radio}} \times [(\zeta = \text{ObTimes}/\text{ObDays})^{-1} \times (\eta = 10^{-5})^{-1} \times (F_b = 0.1)]$.

Li et al. (2021) introduced the detection of 1652 pulses from FRB 20121102A with FAST and proposed a bimodal energy distribution. The calculation there follows Equation (9) from Zhang (2018), which differs from Equation (3) by a constant $\nu_c/\Delta\nu$, if we calibrate the fluence both with the full bandwidth.¹⁴ Aggarwal (2021) claimed that he recalculated the energy using the bandwidth in Table 1 of Li et al. (2021), and the resulting distribution did not show a significant bimodality. As we have demonstrated in Figure 3(A), the specific fluence varies greatly with the bandwidth selection. The calculation in Aggarwal (2021) simply replaced ν_c with the apparent observed bandwidth for individual bursts, but still used the fluence values derived from the full bandwidth to do the calculation. Therefore the calculations of Aggarwal (2021) resulted in incorrect results. The bimodal energy distribution for FRB 20121102A as claimed by Li et al. (2021) remains intact.

3.3. Energy Distribution

Energy/luminosity function can provide important hints on the emission mechanism of the source. As we demonstrated in the previous subsection, the use of limited bandwidth or full bandwidth does not change the energy distribution. Therefore, we uniformly use Equation (2) and the full bandwidth fluence for energy calculation in the following analysis.

As affirmed in Figure 4(C), the energy distribution of FRB 20201124A also presents a clear bimodal distribution, which can be well-fitted by two log-normal functions peaking at 2.27×10^{37} erg and 2.28×10^{38} erg, respectively. This may indicate the existence of more than one emission mechanism to generate FRBs. The distribution of FRB 20121102A could be also fitted by a similar double log-normal distribution (Extended Data Figure 5 in Li et al. 2021), but the peak energies are not the same for the two FRB sources.

¹⁴ The method of Zhang (2018) applies to FRBs with emission bandwidth much wider than the telescope's bandwidth, which seems to be the case for at least some non-repeating FRBs.

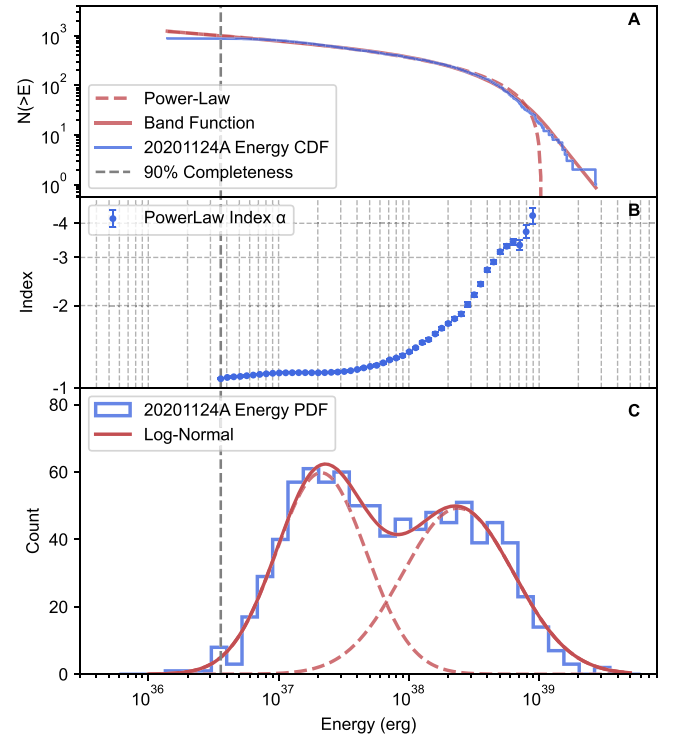


Figure 4. The energy distribution of FRB 20201124A. A: The cumulative energy distribution of FRB 20201124A (blue) with Band function and single-power law function fitting. B: The index of single-power law fitting as a function of energy threshold. C: The energy distribution of FRB 20201124A (blue) with two log-normal fittings.

For a power law energy/luminosity distribution $dN/dE = AE^\alpha$, the cumulative energy distribution can be calculated as

$$\begin{aligned}
 N(>E) &= \int_E^{E_{\text{max}}} dN = \int_E^{E_{\text{max}}} AE^\alpha dE \\
 &= \frac{A}{-\alpha - 1} [E^{\alpha+1} - E_{\text{max}}^{\alpha+1}] = \frac{A}{-\hat{\alpha}} [E^{\hat{\alpha}} - E_{\text{max}}^{\hat{\alpha}}], \quad (3)
 \end{aligned}$$

where E_{max} is the maximum energy for a certain sample, and $\hat{\alpha} = \alpha + 1$. One can see that, in general, the cumulative energy

distribution is also roughly a power law with index $\hat{\alpha}$ being $\hat{\alpha} < 0$. Different types of astrophysical sources have different $\hat{\alpha}$ values. For example, solar flare events have $-0.9 < \hat{\alpha} < -0.5$ (Maehara et al. 2015) and giant pulses of the Crab pulsar have $-2.8 < \hat{\alpha} < -1.1$ (Mickaliger et al. 2012; Lyu et al. 2021). Different repeating FRBs are observed to have different $\hat{\alpha}$ values: e.g., $-1.8 < \hat{\alpha} < -0.7$ for FRB 20121102A (Law et al. 2017; Gourdjji et al. 2019; Cruces et al. 2021), and $\hat{\alpha} \sim -1.3$ for FRB 20180916B (CHIME/FRB Collaboration et al. 2020). For FRB 20201124A, $\hat{\alpha} \sim -1.2$ was measured for the uGMRT bursts (Marthi et al. 2021) and $\hat{\alpha} \sim -3.6$ was measured for the CHIME bursts (Lanman et al. 2022). A broken power law was also used to model the cumulative energy distribution of FRB 20121102A, and the indexes $\hat{\alpha} = -1.4$ and $\hat{\beta} = -1.8$ around the turning point 2.3×10^{37} erg (Aggarwal et al. 2021; Hewitt et al. 2022). The bursts in our FAST sample also require a two-segment power law, but the turning point is not obvious. Therefore, we apply an exponentially connected broken-power law function (which is called the Band function proposed by Band et al. (1993) to describe the gamma-ray spectra of gamma-ray bursts), which reads

$$N(>E) = \begin{cases} AE^{\hat{\alpha}} e^{(-E/E_0)} & E \leq (\hat{\alpha} - \hat{\beta})E_0 \\ AE^{\hat{\beta}} \left[\frac{(\hat{\alpha} - \hat{\beta})E_0}{e} \right]^{\hat{\alpha} - \hat{\beta}} & E \geq (\hat{\alpha} - \hat{\beta})E_0, \end{cases} \quad (4)$$

where $\hat{\alpha} = \alpha + 1$ and $\hat{\beta} = \beta + 1$ are the power law indices of the lower and higher cumulative energy distributions, and E_0 is a characteristic energy. Note that strictly speaking the cumulative energy distribution of two log-normal functions should have a complicated shape. The simple power law function is insufficient. We therefore adopt the next simplest function, i.e., a smoothly joined two-segment broken power law function (the Band function) to fit it. As shown in Figure 4(A), this function fits the data reasonably well. In principle, the turnover in the low-energy end of the low-energy log-normal component would demand an additional break in the function to fit the cumulative distribution and indeed there is a deviation at the low-energy end between the data and fitting function. In any case, when considering possible selection effect near the sensitivity threshold (which would compensate the deficit of low-energy bursts from the data), we believe that the Band function presents a reasonable description of the cumulative distribution function.

We exclude the bursts that are below the 90% detection threshold ($E_{\text{th}} = 3.6 \times 10^{36}$ erg), which make up 1% of the total sample. We then randomly select 90% of the bursts in the sample to generate a cumulative energy distribution. We repeat this process 1000 times and fit these 1000 cumulative energy

distributions with a power law function and the Band function. The central limit theorem makes the fitting parameters converge to a Gaussian distribution. We use the mean and standard deviation of the Gaussian distribution as the standard value and error of the fitting parameters. Figure 4(A) plots the fitting results of the cumulative energy distribution. The power law index is $\hat{\alpha} = -0.08 \pm 0.01$. The index values in the Band function are $\hat{\alpha} = -0.22 \pm 0.01$ and $\hat{\beta} = -3.27 \pm 0.34$, with the turning point at $(1.1 \pm 0.2) \times 10^{39}$ erg. Note that the power law indices and the break energy are all different from those derived from the CHIME bursts. Considering the uncertainties, the index of the higher energy end is consistent with the CHIME result.

We repeat the fitting process with a varying energy threshold. The index $\hat{\alpha}$ of a single-power law function does not converge to a single value in panel B of Figure 4. This is another indication that a single power law distribution is inadequate to describe the cumulative energy distribution of this FRB source.

4. Discussion

4.1. Comparison with other Repeating FRBs

FRB 20121102A, FRB 20190520B and FRB 20201124A are three repeating FRBs which have been extensively studied by FAST. FRB 20121102A is the first known repeating FRB (Spitler et al. 2014, 2016). FRB 20190520B is a repeating FRB detected by Commensal Radio Astronomy FAST Survey (CRAFTS) (Li et al. 2019; Niu et al. 2022b). Both FRB 20121102A and FRB 20190520B are found to be associated with a compact persistent radio source (PRS) (Marcote et al. 2017; Chatterjee et al. 2017; Niu et al. 2022b). FRB 20201124A is also associated with persistent radio emission, but it is not a point source and is rather extended in space (Piro et al. 2021; Ravi et al. 2022). The FAST-measured energy distributions of these three FRB sources can be directly compared against each other to reduce the possible selection biases caused by using different telescope systems. Figure 5 displays the energy distributions of the three FRBs in the form of both power density function (PDF) and cumulative density function (CDF). Both the PDF and CDF show that the energy distributions of the three FRB sources are not consistent.

Table 1 lists the observed isotropic radio energy and the inferred burst energy of the three FRBs. The total observed energy E_{radio} is the sum of all the observed burst energies in the radio band, which is corrected to the total energy released during the bursts via Equation (5).

$$E_{\text{bursts}} = E_{\text{radio}} \times F_b \times \eta^{-1} \times \zeta^{-1}, \quad (5)$$

where E_{bursts} is the total energy emitted by the FRB source during bursts, F_b is the beaming factor, η is the radio efficiency which is normalized to $\sim 10^{-5}$ (similar order to FRB

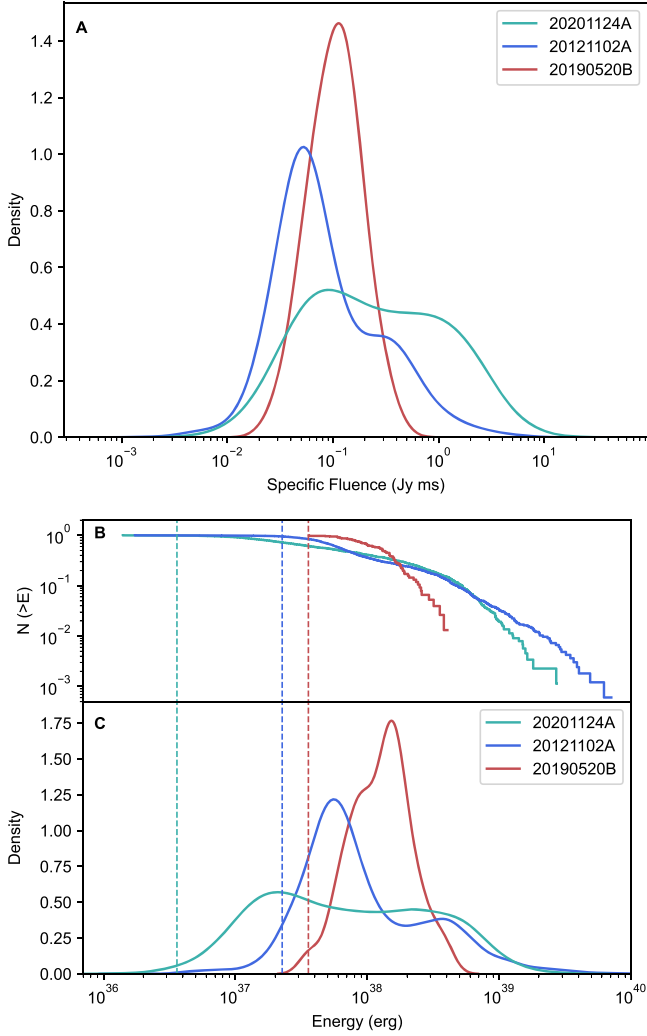


Figure 5. Fluence and energy distribution of FRB 20201124A (green), FRB 20190520B (red) and FRB 20121102A (blue). A is the kernel density estimation (KDE) of the three FRBs’ fluence. B and C are cumulative distributions and KDEs of the three FRBs’ energy. The dashed lines are the detection thresholds.

20200428) and ζ is the observation duty cycle. For example, the observations of FRB 20201124A this time were carried out in four sessions over 4 days with 1 hr per session. The duty cycle ζ is therefore estimated as $(4 \times 1 \text{ hr}) / (4 \times 24 \text{ hr}) = 1/24$.

Compared with other repeaters, FRB 20201124A has the largest averaged energy, especially on September 28. Taking the nominal values of $\eta = 10^{-5}$ and $F_b = 0.1$, the total burst energy released on September 28 reached $(2.46 \times 10^{46} \text{ erg}) \eta_{-5}^{-1} F_{b,-1}$. Compared with the total dipolar magnetic energy of a magnetar $E_{\text{mag}} = (1/6) B_p^2 R^3 \sim (1.7 \times 10^{47} \text{ erg}) B_{p,15}^2 R_6^3$, the burst energy emitted on this day already exceeded 14.3% $\eta_{-5}^{-1} F_{b,-1}$ of the available magnetar energy. This raises an even more severe energy budget problem compared with FRB 20121102A (Li et al. 2021). This requires that the radio

emission efficiency should be quite high for the magnetar model or that the magnetar engine does not apply. For magnetar models, since the synchrotron maser models invoking relativistic shocks are quite inefficient, the data favor magnetospheric models for FRBs, which can have a higher efficiency as observed in radio pulsars (Kumar et al. 2017; Yang & Zhang 2018; Lu et al. 2020; Zhang 2022). The synchrotron maser model may be still relevant if the central engine is not a magnetar, but rather an accreting black hole system (e.g., Sridhar et al. 2021), whose total energy budget is not limited by the total magnetic energy of a magnetar.

4.2. Comparison of Different Burst Definition Schemes

To quantify the specific morphological characteristics of the bursts, we differentiate two kinds of pulse profile classification schemes. The first classification scheme is based on a judgment of pulse flux threshold, taking the pulse profile above the detection threshold as a separated burst. For conservative considerations, we take the detection threshold using a 3σ noise level of the baseline due to the complicated effect on the actual sensitivity, e.g., the bandwidth limited structure of the bursts and radio frequency interference (RFI) events. This definition is also the pulse definition used in previous work, and is the same as the definition used for FRB 20121102A (Li et al. 2021) and FRB 20190520B (Niu et al. 2022b). In the following text, we call this definition Combined Bursts Definition (CBD).

For another method, we try to differentiate the bursts by referring to the morphological clustering characteristics of the pulses in the dynamic spectrum, which means that pulses that can be distinguished in the time-frequency diagram are treated as different bursts, like Figure 6. We call this definition Separated Bursts Definition (SBD). As a result, the event in Figure 6 contains two bursts under SBD but one burst under CBD. All bursts under SBD are artificially isolated and flux calibration is performed independently.

Figure 7(A) depicts the waiting time distribution of bursts with SBD, which is still a bimodal distribution and can be modeled with two log-normal functions peaking at 13.56 ms and 10.05 s, respectively. The second peak time around 10 s is consistent with the waiting time distribution of CBD. However, the first peak time is significantly reduced. The distributions of specific fluence and energy exhibit distinct distributions under the two burst definitions. We apply the K-S test to check whether the energies calculated from the two burst definition schemes belong to the same distribution. The p -value is 0.2%, meaning we could rule out the hypothesis that they were from the same distribution. We also use the Band function to fit the cumulative energy distribution of the bursts with SBD. The index values in the Band function are $\hat{\alpha} = -0.18 \pm 0.01$ and $\hat{\beta} = -3.27 \pm 0.16$. The index in the high energy regime is the same with CBD, while the index in the lower energy regime is slightly smaller than that of CBD. The turning point is

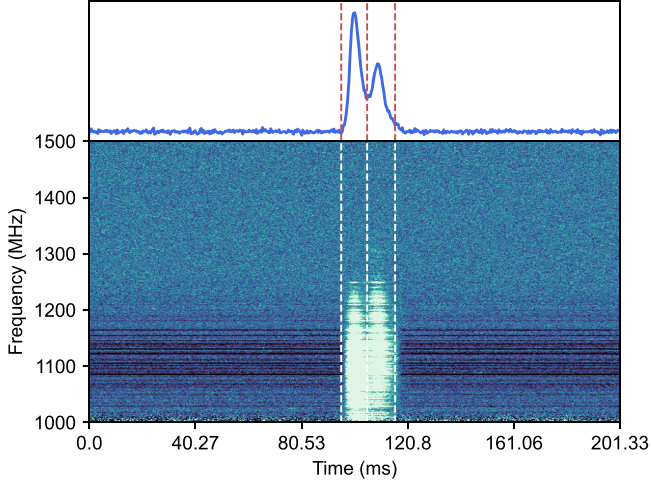


Figure 6. A burst event example detected on September 26.

$(6.4 \pm 0.1) \times 10^{38}$ erg, which is smaller than that for CBD. While we still do not know the true nature of FRBs, different definitions of bursts may lead to somewhat different analysis results. We caution that when studying burst energy distributions of FRBs, one needs to specify a burst definition scheme.

5. Conclusions

FRB 20201124A is a repeating FRB discovered by CHIME (CHIME/FRB Collaboration et al. 2021). FAST monitored this source multiple times. Besides an earlier observational campaign reported by Xu et al. (2021), we study a very active 4 day emitting episode that occurred on 2021 September 25–28, in this series of papers. The main results of this paper are as follows.

1. Using our CBD definition method, a total of 881 bursts were detected between September 25 and 28.
2. The apparent event rate increased exponentially in 4 days and then dropped to zero after September 29.
3. The waiting time of FRB 20201124A shows a bimodal structure, which can be well-fitted by two log-normal functions. The longer waiting times peak around 10 s. This peak waiting time is insensitive to the burst definition criterion. It is much shorter than that of the previous epoch (Xu et al. 2021), suggesting that it is related to the activity level of the source.
4. The shorter waiting times peak around either 51 ms or 14 ms, depending on the definition of burst separation (see Section 3).
5. The peak event rate of 542 hr^{-1} exceeds all the detected FRBs in the past, including 122 hr^{-1} of FRB 20121102A (Li et al. 2021), and FRB 20201124A itself, which was 45.8 hr^{-1} during the last active period (Xu et al. 2021).

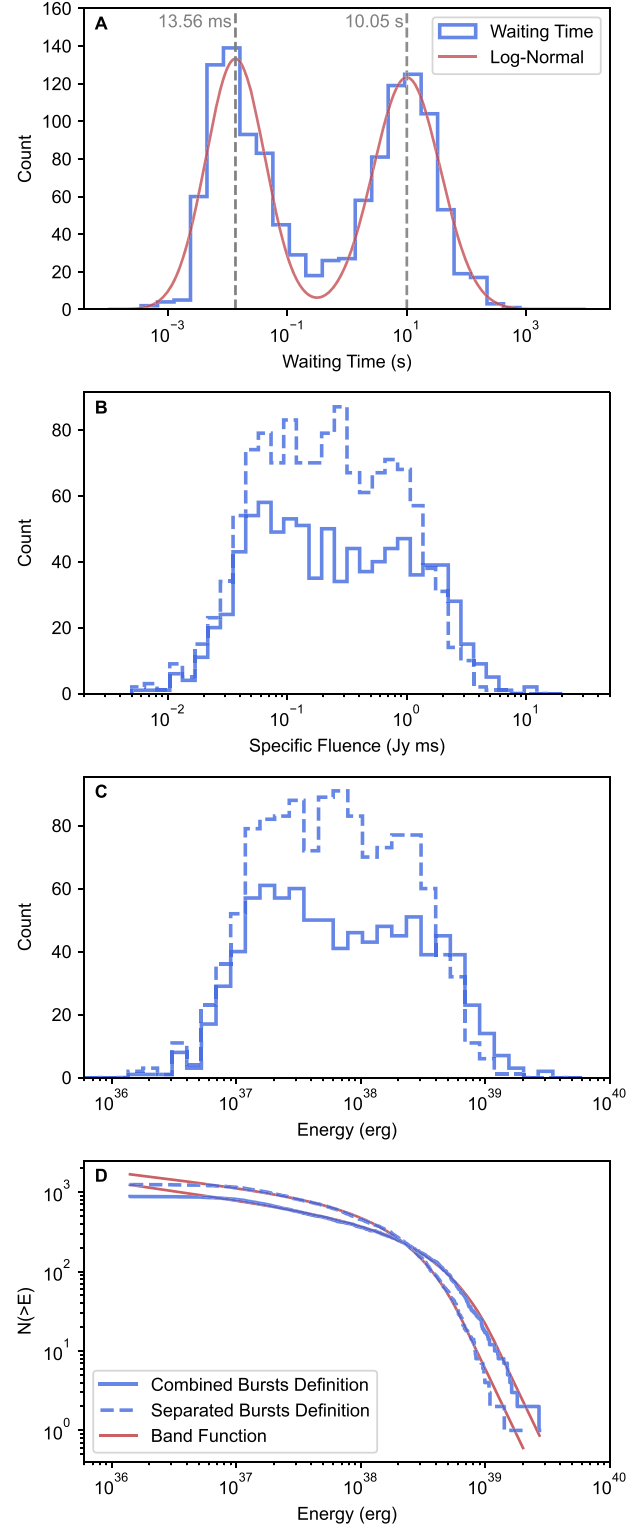


Figure 7. A: Waiting time distribution of the bursts from FRB 20201124A with SBD. The red line shows the log-normal fitting. B: Specific fluence distribution of bursts with CBD (blue solid line) and SBD (blue dashed line). C: Energy distribution of bursts with CBD and SBD. D: Cumulative energy distribution of bursts with CBD and SBD with Band function fitting (red line).

The total burst energy released during this epoch is a significant fraction of magnetar total energy unless the radio emission frequency is high. This challenges the synchrotron maser mechanism for FRBs and even the magnetar source model.

6. The energy distribution cannot be described by a single power law. The cumulative distribution of energy can be well modeled by an exponentially connected broken power law known as the Band function. The slopes at low and high energy regimes are $\hat{\alpha} = -0.22 \pm 0.01$ and $\hat{\beta} = -3.27 \pm 0.23$, respectively.
7. The energy distributions of three active repeating FRBs, namely FRB 20121102A, FRB 20190520B and FRB 20201124A, do not appear to be identical. This suggests that repeating FRBs may have diverse emission properties.

Acknowledgments

This work was supported by the National Natural Science Foundation of China (NSFC, Grant Nos. 11988101 and 11725313). This work made use of the data from FAST, a Chinese national mega-science facility, operated by National Astronomical Observatories, Chinese Academy of Sciences. This work was supported by the Open Project Program of the Key Laboratory of FAST, Chinese Academy of Sciences. We acknowledge use of the CHIME/FRB Public Database, provided at <https://www.chime-frb.ca/> by the CHIME/FRB Collaboration. P.W. acknowledges support from the National Natural Science Foundation of China (NSFC, Grant No. U2031117), the Youth Innovation Promotion Association CAS (id. 2021055), CAS Project for Young Scientists in Basic Research (grant YSBR-006) and the Cultivation Project for FAST Scientific Payoff and Research Achievement of

CAMS-CAS. Y.F. is supported by the Key Research Project of Zhejiang Lab No. 2021PE0AC0. J.L.H. is supported by the National Natural Science Foundation of China (NSFC, Grant Nos. 11988101 and 11833009) and the Key Research Program of the Chinese Academy of Sciences (Grant No. QYZDJ-SSW-SLH021); D.J.Z. is supported by the Cultivation Project for the FAST scientific Payoff and Research Achievement of CAMS-CAS. K.J.L., J.C.J., H.X. and J.W.X. are supported by National SKA Program of China 2020SKA0120200, National Natural Science Foundation of China (NSFC, Grant No. 12041303), the CAS-MPG LEGACY project, and funding from the Max-Planck Partner Group.

Author Contributions

Y.K.Z., P.W., D.L. and B.Z. developed the concept of the manuscript. B.Z. and W.W.Z. proposed and chaired the FAST FRB key science project. Y.K.Z. conducted the data analysis and visualization. Y.K.Z., P.W. and C.H.N. searched the bursts and analyzed the burst properties. Y.K.Z., Y.F., D.L., B.Z., C.W.T. and R.L. led the discussion on the interpretation of the results and writing of the manuscript. D.J.Z. studied burst morphology and classification with the details presented in paper I of this series. J.C.J. performed the analysis of the polarization properties and the results are presented in Paper III. J.R.N. performed periodicity search with the results presented in Paper IV. All authors contributed to the analysis or interpretation of the data and to the final version of the manuscript.

Bursts Properties

Table A1 displays the properties of all 881 bursts. The full table can be found online as supplementary material.

Table A1
The Properties of the FRB 20201124A Bursts

Burst ID	Obs Date	MJD ^a	DM (pc cm ⁻³)	Width ^b Full Band (ms)	Peak Flux Full Band (mJy)	Fluence Full Band (Jy ms)	Energy ^c	Energy ^d	Bandwidth (MHz)	Width ^b Limited Band (ms)	Peak Flux Limited Band (mJy)	Fluence Limited Band (Jy ms)	Energy ^c
		Barycentric					Full Band (erg)	Full Band (erg)					Limited Band (erg)
1	20210925	59482.944514719	412.97	3.31	12.39 ± 0.26	0.04 ± 0.01	1.148(1) e+37	4.590(1) e+36	200	3.81	22.50 ± 0.74	0.09 ± 0.01	4.210(45) e+36
2	20210925	59482.946731974	412.97	3.78	28.61 ± 0.05	0.11 ± 0.01	3.023(28) e+37	1.209(11) e+37	150	3.55	79.38 ± 0.36	0.28 ± 0.01	1.038(10) e+37
3	20210925	59482.947007613	412.97	4.34	5.99 ± 0.07	0.03 ± 0.01	7.278(1) e+36	2.911(1) e+36	50	5.18	32.52 ± 0.22	0.17 ± 0.01	2.071(22) e+36
4	20210925	59482.947121260	412.97	2.70	7.41 ± 0.09	0.02 ± 0.01	5.598(1) e+36	2.239(1) e+36	100	3.54	20.05 ± 0.42	0.07 ± 0.01	1.747(22) e+36
5	20210925	59482.947355910	412.97	4.47	9.61 ± 0.1	0.04 ± 0.01	1.204(1) e+37	4.814(1) e+36	100	4.00	38.02 ± 0.22	0.15 ± 0.01	3.740(45) e+36
6	20210925	59482.947576756	412.97	2.85	10.89 ± 1.93	0.03 ± 0.01	8.677(1) e+36	3.471(1) e+36	150	3.17	22.96 ± 4.26	0.07 ± 0.01	2.687(34) e+36
7	20210925	59482.947690227	412.97	8.46	211.11 ± 1.1	1.79 ± 0.01	5.002(45) e+38	2.001(18) e+38	300	7.82	462.35 ± 2.39	3.62 ± 0.03	2.668(25) e+38
8	20210925	59482.950048429	412.97	5.77	68.47 ± 0.64	0.40 ± 0.01	1.106(11) e+38	4.422(45) e+37	450	5.26	75.19 ± 0.71	0.40 ± 0.01	4.373(40) e+37
9	20210925	59482.952261654	412.97	4.83	29.58 ± 0.28	0.14 ± 0.01	4.003(28) e+37	1.601(11) e+37	200	4.79	67.06 ± 0.66	0.32 ± 0.01	1.581(13) e+37
10	20210925	59482.953261568	412.97	5.96	38.59 ± 0.37	0.23 ± 0.01	6.438(56) e+37	2.575(22) e+37	150	5.30	104.79 ± 1.05	0.56 ± 0.01	2.049(20) e+37

Notes.^a At 1.5 GHz.^b Equivalent width.^c Energy calculated with center frequency.^d Energy calculated with bandwidth.

(This table is available in its entirety in the online supplementary material. The full table can be found at the ISM/CRAFTS website <http://groups.bao.ac.cn/ism/CRAFTS/FRB20201124A/> and ScienceDB <https://doi.org/10.57760/sciencedb.06762.>)

ORCID iDs

Yong-Kun Zhang  <https://orcid.org/0000-0002-8744-3546>
 Rui Luo  <https://orcid.org/0000-0002-4300-121X>
 De-Jiang Zhou  <https://orcid.org/0000-0002-6423-6106>
 Jia-Rui Niu  <https://orcid.org/0000-0001-8065-4191>
 Jin-Chen Jiang  <https://orcid.org/0000-0002-6465-0091>

References

- Aggarwal, K. 2021, *ApJL*, **920**, L18
 Aggarwal, K., Agarwal, D., Lewis, E. F., et al. 2021, *ApJ*, **922**, 115
 Arcus, W. R., Macquart, J. P., Sammons, M. W., James, C. W., & Ekers, R. D. 2021, *MNRAS*, **501**, 5319
 Band, D., Matteson, J., Ford, L., et al. 1993, *ApJ*, **413**, 281
 Bhandari, S., Keane, E. F., Barr, E. D., et al. 2018, *MNRAS*, **475**, 1427
 Chatterjee, S., Law, C. J., Wharton, R. S., et al. 2017, *Natur*, **541**, 58
 CHIME/FRB Collaboration, Amiri, M., Andersen, B. C., et al. 2020, *Natur*, **582**, 351
 CHIME/FRB Collaboration, Amiri, M., Andersen, B. C., et al. 2021, *ApJS*, **257**, 59
 CHIME/FRB Collaboration 2021, ATel, **14497**, 1
 Cruces, M., Spitler, L. G., Scholz, P., et al. 2021, *MNRAS*, **500**, 448
 Fong, W. -f., Dong, Y., Leja, J., et al. 2021, *ApJL*, **919**, L23
 Golpayegani, G., Lorimer, D. R., Ellingson, S. W., et al. 2019, *MNRAS*, **489**, 4001
 Gourdji, K., Michilli, D., Spitler, L. G., et al. 2019, *ApJL*, **877**, L19
 Hashimoto, T., Goto, T., Chen, B. H., et al. 2022, *MNRAS*, **511**, 1961
 Hashimoto, T., Goto, T., On, A. Y. L., et al. 2020b, *MNRAS*, **498**, 3927
 Hashimoto, T., Goto, T., Wang, T. -W., et al. 2020a, *MNRAS*, **494**, 2886
 Hewitt, D. M., Snelders, M. P., Hessels, J. W. T., et al. 2022, *MNRAS*, **515**, 3577
 Hilmarsson, G. H., Spitler, L. G., Main, R. A., & Li, D. Z. 2021, *MNRAS*, **508**, 5354
 Jahns, J. N., Spiliter, L. G., Nimmo, K., et al. 2022, arXiv:2202.05705
 James, C. W., Prochaska, J. X., Macquart, J. P., et al. 2022, *MNRAS*, **510**, L18
 Jiang, J. C., Wang, W. Y., Xu, H., et al. 2022, *RAA*, **22**, 124003
 Jiang, P., Tang, N. -Y., Hou, L. -G., et al. 2020, *RAA*, **20**, 064
 Kumar, P., Lu, W., & Bhattacharya, M. 2017, *MNRAS*, **468**, 2726
 Kumar, P., Shannon, R. M., Lower, M. E., et al. 2022, *MNRAS*, **512**, 3400
 Lanman, A. E., Andersen, B. C., Chawla, P., et al. 2022, *ApJ*, **927**, 59
 Law, C. J., Abuzzo, M. W., Bassa, C. G., et al. 2017, *ApJ*, **850**, 76
 Law, C., Tendulkar, S., Clarke, T., Aggarwal, K., & Bethapudy, S. 2021, ATel, **14526**, 1
 Li, D., Dickey, J. M., & Liu, S. 2019, *RAA*, **19**, 016
 Li, D., Wang, P., Qian, L., et al. 2018, *IMMag*, **19**, 112
 Li, D., Wang, P., Zhu, W. W., et al. 2021, *Natur*, **598**, 267
 Lorimer, D. R., Bailes, M., McLaughlin, M. A., Narkevic, D. J., & Crawford, F. 2007, *Sci*, **318**, 777
 Lu, W., & Kumar, P. 2016, *MNRAS*, **461**, L122
 Lu, W., & Kumar, P. 2019, *MNRAS*, **483**, L93
 Lu, W., Kumar, P., & Zhang, B. 2020, *MNRAS*, **498**, 1397
 Luo, R., Lee, K., Lorimer, D. R., & Zhang, B. 2018, *MNRAS*, **481**, 2320
 Luo, R., Men, Y., Lee, K., et al. 2020, *MNRAS*, **494**, 665
 Lyu, F., Meng, Y. -Z., Tang, Z. -F., et al. 2021, *FrPhy*, **16**, 24503
 Macquart, J. P., & Ekers, R. D. 2018, *MNRAS*, **474**, 1900
 Madau, P., & Dickinson, M. 2014, *ARA&A*, **52**, 415
 Maehara, H., Shibayama, T., Notsu, Y., et al. 2015, *EP&S*, **67**, 59
 Main, R. A., Hilmarsson, G. H., Marthi, V. R., et al. 2022, *MNRAS*, **509**, 3172
 Marcote, B., Paragi, Z., Hessels, J. W. T., et al. 2017, *ApJL*, **834**, L8
 Marthi, V. R., Bethapudi, S., Main, R. A., et al. 2021, arXiv:2108.00697
 Mickaliger, M. B., McLaughlin, M. A., Lorimer, D. R., et al. 2012, *ApJ*, **760**, 64
 Nan, R., Li, D., Jin, C., et al. 2011, *IJMPD*, **20**, 989
 Nicholl, M., Williams, P. K. G., Berger, E., et al. 2017, *ApJ*, **843**, 84
 Nimmo, K., Hewitt, D. M., Hessels, J. W. T., et al. 2022, *ApJL*, **927**, L3
 Niu, C. H., Aggarwal, K., Li, D., et al. 2022b, *Natur*, **606**, 873
 Niu, J. R., Zhu, W. W., Zhang, B., et al. 2022a, *RAA*, **22**, 124004
 Petroff, E., Barr, E. D., Jameson, A., et al. 2016, *PASA*, **33**, e045
 Piro, L., Bruni, G., Troja, E., et al. 2021, *A&A*, **656**, L15
 Pleunis, Z., Good, D. C., Kaspi, V. M., et al. 2021, *ApJ*, **923**, 1
 Ransom, S. M. 2001, PhD thesis, Harvard Univ. Massachusetts
 Ravi, V., Law, C. J., Li, D., et al. 2022, *MNRAS*, **513**, 982
 Schechter, P. 1976, *ApJ*, **203**, 297
 Spitler, L. G., Cordes, J. M., Hessels, J. W. T., et al. 2014, *ApJ*, **790**, 101
 Spitler, L. G., Scholz, P., Hessels, J. W. T., et al. 2016, *Natur*, **531**, 202
 Sridhar, N., Metzger, B. D., Beniamini, P., et al. 2021, *ApJ*, **917**, 13
 Vedantham, H. K., Ravi, V., Hallinan, G., & Shannon, R. M. 2016, *ApJ*, **830**, 75
 Wang, F. Y., & Zhang, G. Q. 2019, *ApJ*, **882**, 108
 Xu, H., Niu, J. R., Chen, P., et al. 2022, *Natur*, **609**, 7928
 Yang, Y. -P., & Zhang, B. 2018, *ApJ*, **868**, 31
 Zhang, B. 2018, *ApJL*, **867**, L21
 Zhang, B. 2020, *Natur*, **587**, 45
 Zhang, B. 2022, *ApJ*, **925**, 53
 Zhang, R. C., & Zhang, B. 2022, *ApJL*, **924**, L14
 Zhang, R. C., Zhang, B., Li, Y., & Lorimer, D. R. 2021, *MNRAS*, **501**, 157
 Zhou, D. J., Han, J. L., Zhang, B., et al. 2022, *RAA*, **22**, 124001